Earth and Planetary Science Letters 577 (2022) 117273

Contents lists available at ScienceDirect

Earth and Planetary Science Letters

www.elsevier.com/locate/epsl

What comes first: The fault or the ductile shear zone?

Christopher H. Scholz [a,*], Eunseo Choi [b]

[a] Lamont-Doherty Earth Observatory, Columbia University, Palisades, NY 10964, USA
[b] Center for Earthquake Research and Information, 3890 Central Ave., Memphis, TN 38152, USA

ARTICLE INFO

Article history:
Received 30 June 2021
Received in revised form 20 October 2021
Accepted 27 October 2021
Available online 9 November 2021
Editor: J.-P. Avouac

Keywords:
faults
shear zones
strain weakening
earthquakes
brittle-ductile transition

ABSTRACT

Crustal scale fault zones extend below the brittle-ductile transition as ductile shear zones. Here we address the question of which regime, brittle or ductile, initiates and controls the overall system of shear localization. Observations of crustal scale but low displacement conjugate strike-slip faults show that they are typically nearly orthogonal, as expected from plastic shear criteria. Sub-crustal scale conjugate strike-slip faults, however, have acute dihedral angles in accordance with the Coulomb fracture criterion as Anderson's theory predicts. We modeled the crustal scale system with strain weakening rheologies that follow the Coulomb and von Mises criteria respectively, within the brittle and ductile regimes. We find that when the strain weakening rate in the ductile regime exceeds a critical value the entire system shears in the von Mises mode with orthogonal conjugate shears forming at all depths, in accordance with the observations. There is, as observed, no deflection of fault orientation at the brittle-ductile transition. Anderson's theory of faulting thus breaks down for crustal scale faults. This difference in behavior was already evident in data presented in Anderson's 1951 book, but its significance was not understood at that time.

1. Introduction

It is now recognized that crustal scale continental faults continue downwards as ductile shear zones [e.g., Norris and Toy, 2014; Sibson, 1983]. Such shear zones, exposed in deeply exhumed crust, consist of mylonite belts that can be as large as hundreds of kilometers in length and tens of kilometers in width [e.g. LeLoup et al., 1995]. Direct evidence of deformed mantle peridotites as well a seismic reflections and seismic anisotropy indicate that these shear zones may extend into the upper mantle [Vauchez et al., 2012]. In the case of the particularly well studied San Andreas fault, evidence for its deep ductile root comes from seismic profiles that show it continuing downwards, offsetting the lower crust well below the seismogenic depth [Parsons, 1998]. This deep shear zone tracks the San Andreas on its sinuous path, as indicated by shear wave splitting data that shows a fast direction in the lower lithosphere that follows the surface trace of the fault [Bonnin et al., 2010], a conclusion also supported by geodetic data [Traore et al., 2014; Yamasaki et al., 2014] that show that a low-viscosity zone of finite width underlies major strike-slip faults and extends to considerable depths in the crust. This leads to a tectonic model in which the fault is loaded by interseismic shearing in the deep ductile shear zone which also dominates postseismic relaxation by deep afterslip and flow.

The question arises: how did this situation develop? One can envisage a model in which a fault initiates in the brittle crust and grows to rupture throughout the seismogenic thickness, whereupon its basal shear stress concentration initiates ductile yielding which, by a combination of strain localization mechanisms [e.g., Rutter, 1999], produces a ductile shear zone which then propagates to depth through the lithosphere [e.g. Moore and Parsons, 2015]. On the other hand, one can also envisage the converse, in which the ductile shear zone forms at depth first [e.g. Regenauer-Lieb and Yuen, 2004] and the stress concentration at its upper edge initiates faulting at the base of the brittle layer which then propagates upwards. So, we have two coupled shear systems, one ductile, below the brittle-ductile transition, and one brittle, above it. In the terminology of coupled mechanical systems, the question we are asking is: which is the master and which is the slave?

If the brittle regime dominates, the initial formation of the fault will guide the location and orientation of the shear zone, and if the ductile, then vice versa. This provides a way to distinguish between these possibilities. A fault obeys the Coulomb criterion and forms at an angle $\hat{\theta} = \frac{\pi}{4} - \frac{\tan^{-1}\mu}{2}$ to the maximum compression σ_1 whereas a shear zone follows the Tresca or Von Mises criterion and forms in the plane of maximum shear stress, at 45° to σ_1. However, since we do not usually have an independent way of knowing

* Corresponding author.
E-mail address: scholz@ldeo.columbia.edu (C.H. Scholz).

https://doi.org/10.1016/j.epsl.2021.117273

the σ_1 direction, to distinguish these possibilities we need to study cases of conjugate pairs of faults, for which we can be assured that σ_1 bisects the dihedral angle between the faults. The dihedral angle in the compressional quadrant will be $\hat{\theta}_C = \frac{\pi}{2} - \tan^{-1}\mu$ in the brittle case and 90° in the ductile case. For formation of a new fault, μ is the coefficient of friction for fresh rock, which laboratory measurements [Byerlee, 1978] and deep borehole stress measurements [e.g. Townend, 2006] indicate to be in the range 0.5-0.9, which give a range of $\hat{\theta}_C$ of 63-48°, easily distinguishable from the ductile case. Because fault strikes are more readily measured than dips (which also may vary with depth, an added complication), this test is best made with conjugate pairs of strike-slip faults.

Thatcher and Hill (1991) pointed out that many sets of conjugate strike slip faults are nearly orthogonal. They discussed several possible explanations for this observation, one of which is that the ductile shear zone is the driver, as discussed above, but did not come to any firm conclusions. Here we will make a fuller investigation of this problem, in which we will conclude that by far the most likely conclusion is that ductile shear zones at depth guide the formation of major crustal scale faults. We then investigate the conditions necessary for this to occur.

2. Observations of conjugate strike-slip faults

We observe three distinct classes of strike-slip faults in which their rupture behavior depends on their length scale relative to the width of the brittle regime, $W*$ (10-15 km). Class 1 faults are sub-crustal scale faults, of length $L < W^*$ that propagate entirely within the brittle regime. The dihedral angles of conjugate sets of class 1 faults are found to be, apparently without exception, acute – consistent with the Coulomb fracture criterion. Class 2 faults ($L > W^*$) are crustal scale but low displacement faults. These faults, tens of kms long, have ruptured through the entirety of the brittle regime and hence are likely to coexist with a ductile shear zone at depth, but have undergone little rotation since formation. Conjugate sets of Class 2 faults are found to typically be nearly orthogonal, consistent with ductile shearing criteria. Class 3 faults ($L >> W^*$) are crustal scale faults with large displacements. Conjugate sets of these fault, with lengths of hundreds of kms, often have dihedral angles considerably greater than 90° as a result significant rotation or other reorganization since formation. In the following section, we will provide examples of these fault classes, with emphasis on the second, which illustrates the physics we are interested in here.

The concept of conjugate faults implies that the faults are of contemporaneous origin. To insure this, we consider only fault sets that are currently active seismically. Fig. 1 shows an example used by Thatcher and Hill, the Izu Peninsula of Japan, which, as a part of the Philippine Sea Plate, is colliding in a NNW direction with Honshu, a part of the Eurasian Plate. The rupture zones of all large strike-slip earthquakes since 1930 are shown. In this case, the σ_1 direction can be determined independently from the faulting as being parallel to the alignment of parasitic eruptions, indicated by rows of circles, which mark the surface manifestations of dikes emanating from the active volcanoes [Nakamura, 1969]. These bisect the fault strikes, which are seen to be orthogonal to one another. To the southwest, the fault zones indicate that σ_1 has there rotated to a more northerly direction.

Fig. 2 shows a portion of the active fault map of Japan for the region of southwestern Honshu [AIST, 2015]. This region is dominated by a conjugate set of strike-slip faults. The NNW-SSE trending ones are left-lateral (red), while the ENE-WSW trending ones are right-lateral (black). They indicate a common WNW-ESE σ_1 direction and are nearly orthogonal to one another. The spacing of the right-lateral set is of the order of W^* whereas the left lateral faults are more widely spaced.

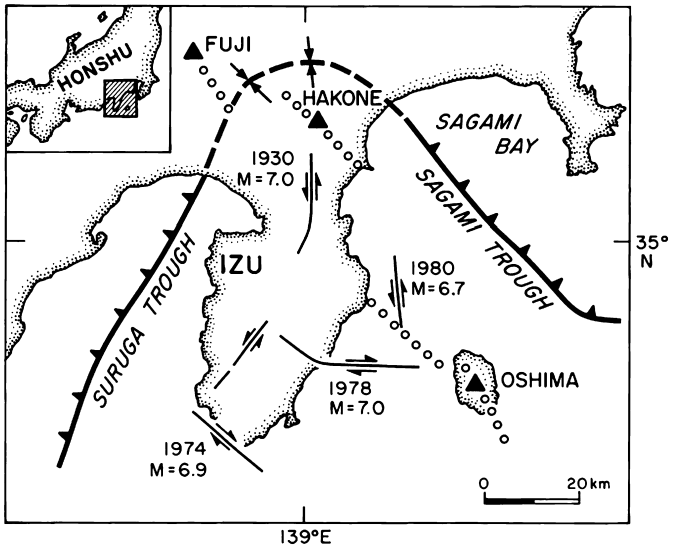

Fig. 1. Map of the Izu Peninsula, Japan, showing major active tectonic elements. Curves with dates are the ruptures of major historic strike-slip earthquakes. Rows of circles indicate the alignment of parasitic eruptions emanating from active volcanoes. From Scholz (2019, p. 99).

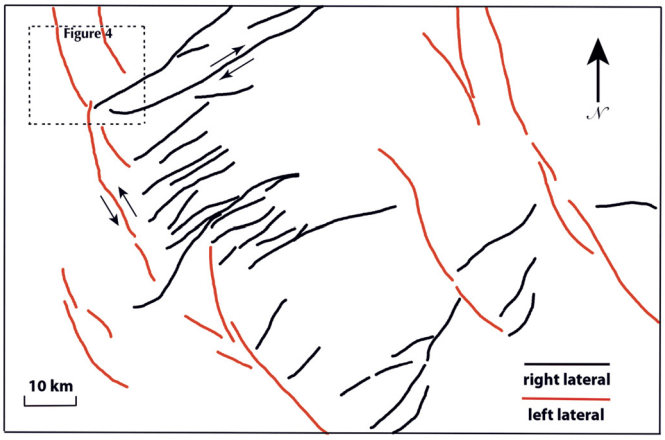

Fig. 2. Map of active strike-slip faults in Central Japan. The NNW-SSE trending ones are left-lateral (red), while the ENE-WSW trending ones are right-lateral (black). From AIST (2015). (For interpretation of the colors in the figure(s), the reader is referred to the web version of this article.)

Earthquakes often rupture conjugate faults, either in a single complex rupture or in a sequence of large earthquakes over a short time interval. Schematic diagrams of strike-slip earthquake ruptures on conjugate faults are shown in Fig. 3. In all these cases the faults are close to orthogonal. The 1927 Tango, Japan earthquake (Fig. 3A) ruptured both the left-lateral Gomura and right-lateral Yamada faults [Matsu'ura, 1977; Tsuboi, 1933]. The 1987 Elmore Ranch earthquake, Fig. 3C, ruptured a cross-fault orthogonal to the San Andreas fault system, followed 12 hours later by the Superstition Hills earthquake on the fault of the same name parallel to the San Andreas. A second cross-fault activated by the Westmoreland earthquake of 1981 is shown as a dashed line in Fig. 3C. Such orthogonal cross-faults are common in the southern San Andreas system [Nicholson et al., 1986; Ross et al., 2017]. A more recent case, the Ridgecrest earthquake of 2019, is shown in Fig. 3D.

Closer inspection reveals that the dihedral angles θ_C in most of these cases are slightly obtuse (Table 1). Because displacements on faults will cause them to rotate away from the σ_1 direction [Freund, 1974; Martel, 1999], the observed θ_C should be larger than its original value $\hat{\theta}_C$. Thatcher and Hill entertained the idea that

Table 1
Conjugate strike-slip fault sets.

Faults	Figure	θ_C	Reference
Central Japan	2,4	101±2°	[AIST, 2015]
Tango, 1927	3A	95±2°	[Matsu'ura, 1977; Tsuboi, 1933]
Sigacik Bay, Turkey, 2005	3B	100±5°	[Aktar et al., 2007]
Elmore Ranch/Superstition Hills, CA, 1987	3C	96±2	[Hudnut et al., 1989]
Ridgecrest, CA, 2019	3D	83±2	[Ross et al., 2019]
Wharton Basin, 2000	3E	92±5	[Robinson et al., 2001]
Wharton Basin, 2012	3F	85±5	[Hill et al., 2015; Yue et al., 2012]
E. and N. Anatolian		116±2	[Simao et al., 2016]
San Andreas/Garlock		125±5	[Hatem and Dolan, 2018]

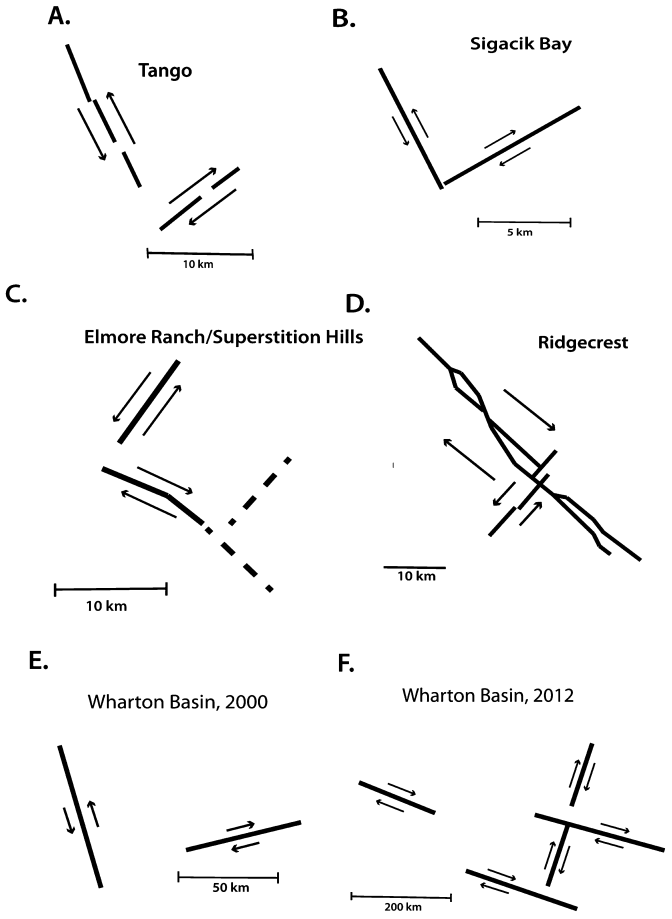

Fig. 3. Maps of conjugate strike-slip earthquake ruptures. Sources listed in Table 1.

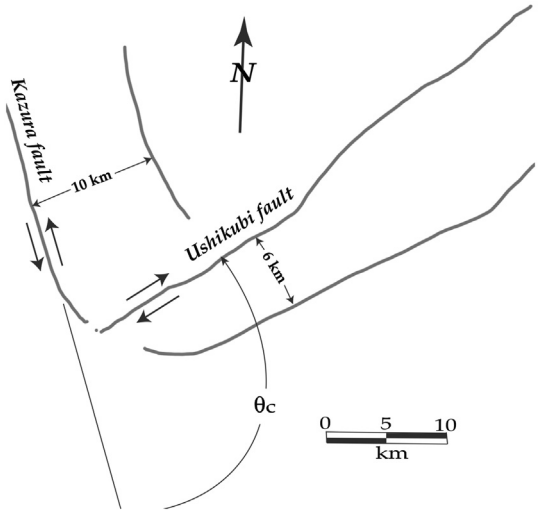

Fig. 4. Close-up from Fig. 2, illustrating the calculations of fault rotation given in the text.

the faults may have originally formed in the Coulomb orientations but subsequent rotation resulted in the approximately orthogonal relationships now seen. We show in Fig. 4 a close-up of a section of Fig. 2 in which the displacements on the faults are known: 2 km on the right lateral Ushikubi fault, and 1 km on the left lateral Kazura fault [AIST, 2015]. If we assume that the faults are free to rotate kinematically as blocks (i.e., bookshelf faulting), we can use, from Freund (1974),

$$\frac{u}{b} = \frac{\sin r}{\cos s \cos(s+r)} \tag{1}$$

where u is fault displacement, b is the width of the block, s is the assumed original angle of the fault from the σ_1 direction, and r is the angle of rotation. Assuming the von Mises criterion for initial fault formation, $s = 45°$. The block width of the Ushikubi fault is 6 km and that of the Kazura fault is 10 km: the results are that the Ushikubi fault has rotated 8° CCW and the Kazura fault 3° CW, resulting in $\theta_C = 101°$, in excellent agreement with the measured value, 101±2°. Alternatively, assuming the Coulomb criterion with $\mu = 0.6$, then $s = 30°$ and we get rotations of 12 and 4°, respectively, and predict $\theta_C = 76°$. This allows us to reject the assumption of the initial orientation being controlled by the Coulomb criterion.

If, instead, we assumed the faults are constrained to rotate elastically, we can use, from Martel (1999),

$$r = \tan^{-1}\left\{\frac{\Delta\tau}{2G}(1-2\upsilon)\right\} \tag{2}$$

where $\Delta\tau$ is stress-drop, G is shear modulus and υ is Poisson's ratio. For a strike slip fault, using $\Delta\tau = \frac{2G}{\pi}\frac{u}{W*}$, where $W*$ is the seismogenic width, 10 km in this case, we find that the Ushikubi fault should have rotated 2° CCW and the Kazura fault 1° CW, and predict $\theta_C = 93°$ *or* 63° for the von Mises or Coulomb cases, respectively. Bookshelf faulting with the von Mises assumption is the only acceptable solution, which indicates that $\hat{\theta}_C$ was approximately 90°, confirming that these faults must have been guided by ductile shear zones at depth.

In the examples given in Fig. 3 A-D, all the faults involved have lengths of only a few tens of kms, similar to those in Fig. 4. Therefore, their net displacements must be on the order of a km or so, judging from fault scaling laws [Scholz, 2019, pp. 106-112], so their rotations must be similar to those calculated in the above example. The evidence thus strongly favors the hypothesis that $\hat{\theta}_C$ in all these cases was $\sim$ 90°. Very long faults with major displacements, such as the North and East Anatolian faults and the San Andreas and Garlock faults, may of course undergone much larger rotations, and this is reflected in their much larger values of θ_C, as listed in Table 1. The angular relations of such major faults may reflect much more complex histories than simple rotation [cf. Hatem

and Dolan, 2018]. Because such fault histories are non-unique, it is not feasible to estimate $\hat{\theta}_C$ for such large displacement faults.

Another option to be considered is that the faults have very low friction. The weakest known faults have $\mu \sim 0.2$ [Collettini et al., 2019; Scholz, 2019, pp. 151-159], which would predict $\hat{\theta}_C = 77°$. If this low a friction is assumed, our earlier calculations of rotations show that the case for Coulomb failure would be only slightly more plausible. The dynamic weakening mechanisms resulting from frictional heating at seismic slip velocities [e.g. Di Toro et al., 2011] are also not applicable in this case because these cannot operate until faults are fully formed and long enough to host large earthquakes. In any case these thermal weakening mechanisms affect dynamic friction whereas fault formation is controlled by the static frictional strength, which deep borehole stress measurements show are defined by strong faults with hydrostatic pore pressure gradients and $0.6 \leq \mu \leq 1.0$ [e.g. Townend, 2006]. So, the weak fault hypothesis is not a plausible explanation for the orthogonal nature of conjugate strike-slip faults.

Studies of smaller than crustal scale conjugate strike-slip faults, on the other hand, find values of θ_C ranging from 40-60°, consistent with the Coulomb criterion and indicating $0.6 \leq \mu \leq 1.2$ [J.L. Anderson et al., 2013; Kelly et al., 1998; Nixon et al., 2011; Peacock and Sanderson, 1995]. These observations show that the alternatives considered above must be incorrect: the operative failure criterion for the brittle regime is indeed the Coulomb criterion with a friction value in the Byerlee range. Thus Anderson's (1905, 1951) theory of faulting fails only at the crustal scale. We suppose that this must result from interactions with ductile shear zones at depth.

3. Numerical modeling

We construct numerical models to investigate the effects of the strain weakening rates in the ductile regime and brittle regime on θ_C. Faults in the brittle regime and shear zones in the ductile regime are both represented with strain localization in the form of shear bands. Strain localization in the ductile regime is induced by strain-weakening rheologies [Gueydan et al., 2014] implemented in an open-source geodynamic simulation code, DES3D (Dynamic Earth Solver in 3D) [Choi et al., 2013; Tan et al., 2013]. The brittle strain localization is enabled by linear reduction of cohesion proportional to the amount of permanent strain [Choi et al., 2013]. The model domain is a $100 \times 100 \times 30$ km box discretized into tetrahedra with an edge length of about 3 km (Fig. 5A). The kinematic boundary conditions are applied such that the pure shear condition is realized: Symmetric shortening at the full rate of 6.3 cm/yr along x direction and extension at the same full rate along y direction. The bottom boundary has the free-slip conditions and the top boundary is a free surface. The initial temperature increases linearly with depth from 0 to 650°C while being laterally uniform. This linear geotherm sets up a rheological layering with the BDT depth of about 15-20 km ("incipient" in Fig. 5B), which typically shallows as ductile weakening progresses ("mature" in Fig. 5B). The top and bottom temperatures are fixed at the initial values and zero heat flux is assumed on the side walls. The models are run until two shear bands growing out of the initial weak zone are stably established, which typically occurs after about 20 kyrs. Full descriptions of the model setup and the depth-averaged measurement of θ_C are provided in the Supplementary Information.

4. Model results

Our models show that θ_C is most sensitive to how fast ductile strain weakening occurs relative to brittle weakening. The faster the brittle weakening is relative to the ductile weakening, θ_C approaches 60°. The model shown in Fig. 5C has the brittle weakening rate (r_b; see Supplementary Materials for definition) of 2 GPa/strain and the ductile rate (r_d) of 0.008 GPa/strain ($r_d/r_b = 0.004$); and shows θ_C of 64°. In this model, the depth distribution of shear stress before strain localization is similar to the incipient profile in Fig. 5B but the relatively fast weakening in the brittle regime allows brittle faults to be dominant in the sense that they can induce ductile strain localization. The model in Fig. 5D has r_b of 0.2 GPa/strain and r_d of 0.08. This model shows θ_C of 80° and has r_d/r_b of 0.4 meaning that the ductile weakening is faster than in Fig. 5C relative to the brittle weakening by two orders of magnitudes. As implied by θ_C close to the von Mises angle, the relatively fast ductile weakening allows ductile shear bands to be dominant. When neither of brittle and ductile shear localization is dominant, θ_C takes an intermediate value between the Coulomb and the von Mises angle.

A systematic investigation of the effects of r_b and r_d on θ_C confirms the importance of their relative magnitudes (Fig. 6A). For r_b of 2 GPa/strain, θ_C is less than 65°, nearly the Coulomb angle, when $r_d < 0.08$ GPa/strain (Fig. 6A); and >85°, nearly the von Mises angle, when r_d is 0.8 GPa/strain. θ_C takes an intermediate value of 72° when r_d is 0.08 to 0.2 GPa/strain. In all cases, θ_C shows a depth variation of about 1°, which indicates that two different preferred orientations would not coexist in our models. When the brittle weakening is slower by an order of magnitude ($r_b = 0.2$ GPa/strain), almost orthogonal shear bands form at r_d as low as 0.2 GPa/strain while θ_C close to the Coulomb angle are seen only when $r_d \leq 0.2$ GPa/strain. For a faster brittle weakening ($r_b = 10$ GPa/strain, θ_C greater than 85° is not observed for any considered values of r_d and θ_C are less than 70° even in the intermediate range of r_d. Within the ranges of r_d and r_b considered in this study, θ_C values do not show any sensitivity to the magnitude of driving strain rates. When measured after the same amount of total boundary displacements, θ_C did not change for twice greater or smaller driving strain rates.

Effects of greater elastic moduli in the lower crust are not as significant as those of the plastospheric weakening rates. Seismic velocities in the crust generally increase with depth, reflecting increasing density and elastic stiffness. The expected effect of a stiffer lower crust is to let strain localization in the ductile regime start earlier because of faster viscoelastic stress buildup there than in a uniform-stiffness model. A group of models ("stiffer lower crust" in Fig. 6B) have 1.5 times greater elastic moduli and a density of 3000 kg/m^3 in the lower half of the domain. This configuration corresponds to about a 20% increase in P and S wave speeds in the lower half of the crust. θ_C in those models shows little difference from the uniform-stiffness case approaching the Coulomb and the von Mises angle when r_d is sufficiently small or large (Fig. 6B). However, θ_C for $r_d = 0.08$ GPa/strain is 68°, meaningfully closer to the Coulomb angle than the corresponding θ_C of the uniform-stiffness case. This apparent dominance of brittle faulting can be attributed to elastic stress buildup occurring at an increased rate in the lowermost part of the brittle layer, which is a part of the stiffened lower half of the domain.

Effects of inelastic volume change accompanying brittle deformation [e.g., Kranz and Scholz, 1977] in the brittle regime are similarly minor. In a model with kinematic boundary conditions, the inelastic volumetric strain will increase pressure, thus normal stress, on a potential shear band. This effect can impede the growth of faults in the brittle regime, potentially promoting the dominance of ductile shear zones. In a set of models ("dilational upper crust", inelastic volumetric strain is computed as $\epsilon_{ps} \tan\psi$, where ψ is the dilation angle. ψ is set to be 30° initially and linearly reduced to 0° as ϵ_{ps} increases from 0 to 5%. As seen in Fig. 6B, this effect is results in θ_C becoming 66° and 81° for the slowest and fastest ductile weakening; and 76° for the intermedi-

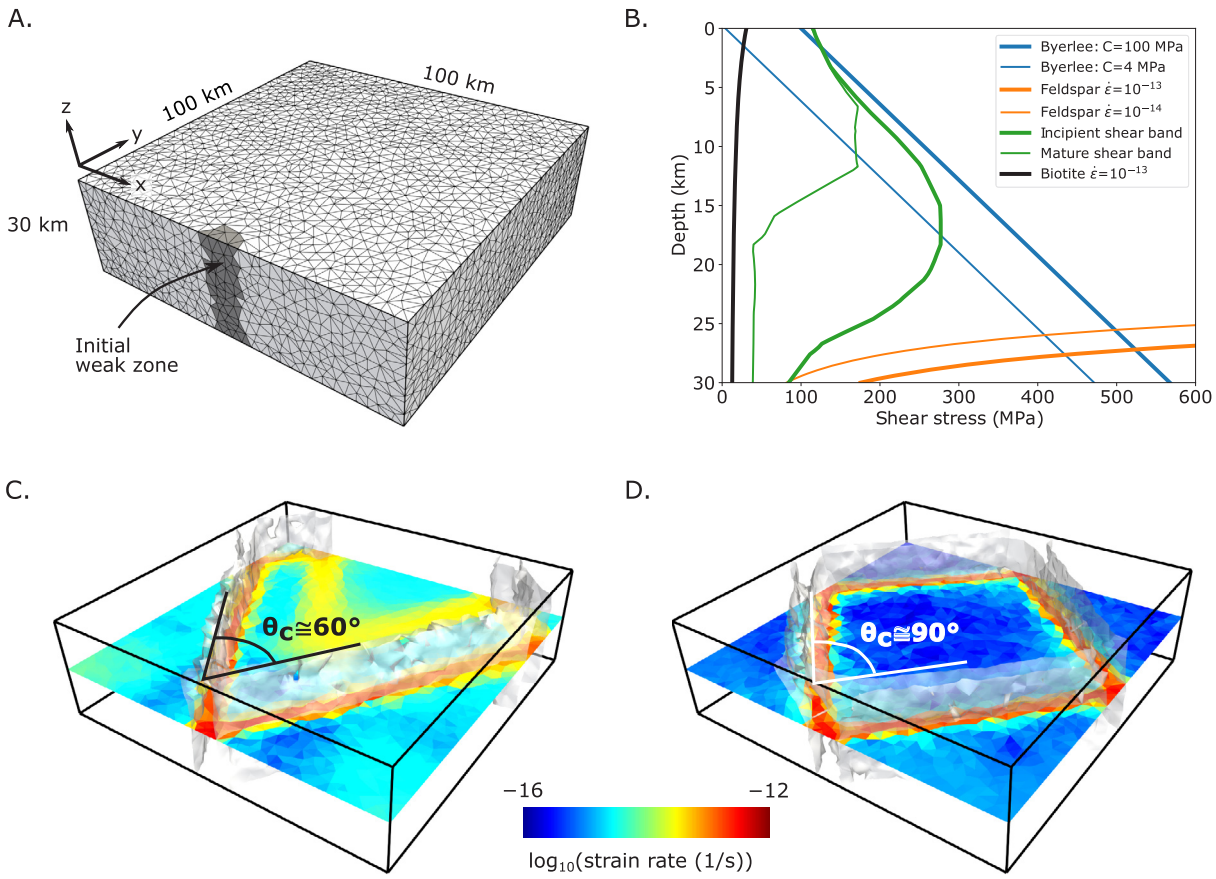

Fig. 5. A. Model domain and mesh with dimensions and coordinate axes. Dark gray elements are weaker than the surrounding to become the starting location of strain localization. **B**. Shear stress profiles for the Byerlee's law and for feldspar [Rybacki and Dresen, 2000] and biotite [Kronenberg et al., 1990] dislocation creep. Also plotted are the profiles of the square root of the second invariant of deviatoric stress from a model with $r_b = -0.2$ GPa/strain and $r_d = -0.08$ GPa/strain. In this model, elastic moduli are uniform and brittle volumetric strain is not included. Profiles were taken at a location where a shear band from the initial weak zone meets the left boundary after 630 m of total boundary displacement ("incipient shear band") and 1890 m ("mature shear band"). **C**. The second invariant of strain rate on the 15 km depth section and the isosurface of the second invariant of strain rate corresponding to $10^{-13.25}$ 1/s from a model with $r_b = -2$ GPa/strain, $r_d = -0.008$ GPa/strain, in which the faulting in the brittle regime is dominant. The dihedral angle (θ_C) of shear bands growing out of the initial weak zone is 64°. **D**. Same with **C** but for a model with $r_b = -0.2$ GPa/strain, $r_d = -0.08$ GPa/strain, in which $\theta_C = 80°$.

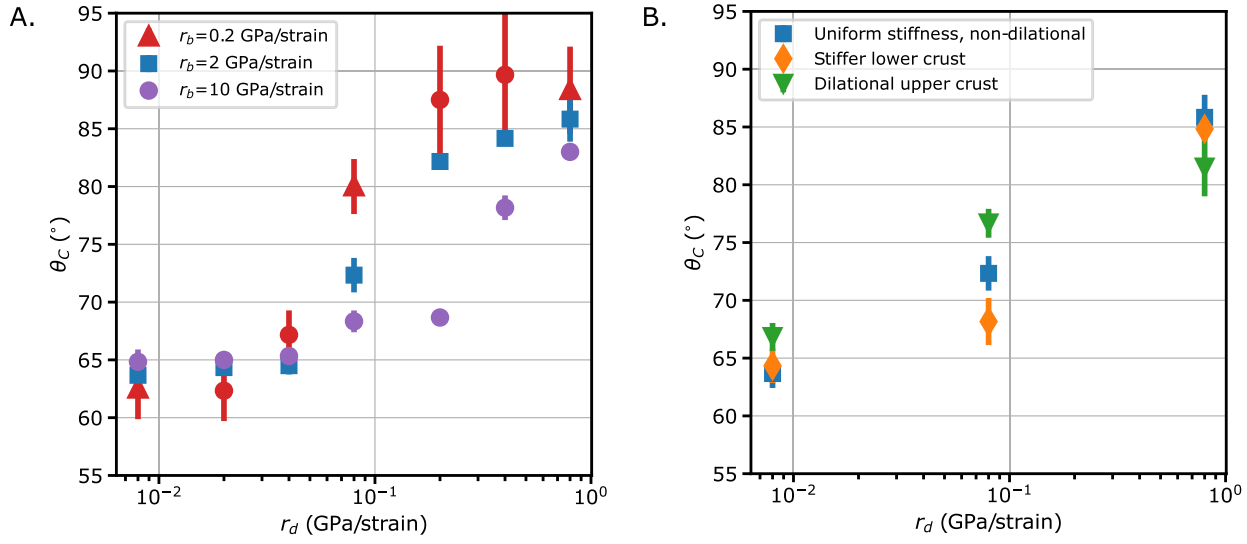

Fig. 6. A. θ_C plotted against the ductile weakening rates (r_d) for different values of the brittle weakening rate (r_b), 0.2, 2 and 10 GPa/strain. Bars on the markers show the depth variations of θ_C. In all cases, the crust has uniform elastic stiffness and inelastic deformations in the brittle regime are non-dilational. **B.** Same as **A** but showing θ_C's for a uniform, non-dilational crust with $r_b = 2$ GPa/strain shown in **A** as well se those for stiffer lower crust and dilational upper crust.

ate r_d. At the two extremes, the main effect is small reduction of the value of θ_C from the von Mises angle at the upper value of r_d.

A recent study by Liang et al. (2021) showed that in their model orthogonal shear zones in the ductile regime can dominate and induce orthogonal faulting in the brittle regime only when fault nucleation starts deep within the ductile layer and the brittle layer is thinner than the ductile one. The first condition is consistent with our results in that nearly orthogonal faults in the brittle layer require ductile shear zones to become dominant before their brittle counterparts do. We employed strain weakening constitutive laws for both brittle and ductile deformations and assumed a geotherm that puts the brittle-ductile transition at around the middle depth. Since strain localization can initiate and evolve spontaneously at any depth in our models, it was the rate of weakening that becomes the primary control parameter, not the relative thickness of brittle layer and prescribed depth of rupture initiation. Another difference is that variation in θ_C with depth is capped by $\pm 4°$ in our study, much smaller than 10-20° rotation seen in their study. The more realistic rheologies used in our models seem to allow one type of strain localization to induce the other more easily.

5. Discussion

Some constraints can be put on the reasonable range of brittle and ductile weakening rates. The brittle strain weakening rate r_b from laboratory measurements on granite is about 2-20 GPa/strain [Lockner et al., 1992], overlapping with the middle to upper level we modeled. At r_d of 0.8 GPa/strain, the greatest value considered in this study, a strength reduction of about 300 MPa occurs after a strain of about 40%. This rate of weakening is apparently faster than the one observed in the original experiments on mica-bearing gneiss [Holyoke and Tullis, 2006]. In those experiments, significant weakening by interconnecting mica occurred over 50-60% of strain but only after a hardening phase over a similar amount of strain. The models with such large values of r_d tend to have a brittle layer much thinner than the typical brittle regime thickness of 10-15 km. Our results show that slower weakening in both regimes can produce nearly orthogonal ($\theta_C \geq 80°$) conjugate faults in a 7 km-thick brittle layer when $r_b = 2$ GPa/strain and $r_d = 0.2$ GPa/strain; and in a 11 km-thick brittle layer when $r_b = 0.2$ GPa/strain and $r_d = 0.08$ GPa/strain (Fig. S2). These values of r_d are comparable to those seen in the experiments. For instance, 0.08 GPa/strain, ductile weakening of 100 MPa would take about 120% of strain. However, it should be noted that the approximating assumptions for the r_d estimation (see "Weakening Rates" in Supplementary Information) makes it difficult to compare model and experimental ductile weakening rates directly. In addition, the experimentally determined r_b and r_d cannot be taken as firm constraints given the uncertainties associated with the extrapolation of lab conditions to the natural ones.

Anderson (1951), in explicating his theory of faulting based on the Coulomb criterion, provided examples from faults in Great Britain. He gave examples of km-scale faults in South Pembrokeshire that beautifully demonstrate his theory [Anderson, 1951, p. 61]. However, the crustal scale faults he discussed behave quite differently. These are the NE trending sinistral strike-slip faults of the Scottish Highlands, of which the Highland Boundary fault and the Great Glen fault are most prominent. The Great Glen fault has at least 100 km of left lateral displacement [Watson, 1984] and has been imaged extending into the mantle [Brewer et al., 1983]. There is a less developed set of dextral strike-slip faults that strike NW and are orthogonal to the NE faults (Fig. 7). Both sets of faults were active in the late Caledonian and have been considered by Anderson and subsequent geologists to be conjugate. The most prominent of the NW faults are the Loch Maree and the Lock Shin-Strath Fleet fault systems. The Loch Shin system is believed to follow the course of a ductile shear zone in the lower crust [Holdsworth et al., 2015; Watson, 1984], and the Lock Maree fault is found to appear as a ductile shear zone where it is exposed in the Lewisian basement [Johnstone and Mykura, 1989]. There it is observed to be a belt of mylonites intercalated with occasional pseudotachylytes; an association which places it at a level not far below the brittle-ductile transition [Aharonov and Scholz, 2019]. The Great Glen and Highland boundary faults similarly follow the line of ductile shear zones at depth [Watson, 1984]. We thus see, in these cases, transitions from ductile shear zones to strike-slip faults, in which the faults are a palimpsest of the underlying pattern of shear zones. This is a direct observation of what is expected from our models in which ductile shearing at depth precedes and drives brittle faulting. A similar set of crustal scale conjugate strike-slip faults overlying orthogonal ductile shear zones is observed in the southern Bavarian Massif of Austria [Brandmayr et al., 1995].

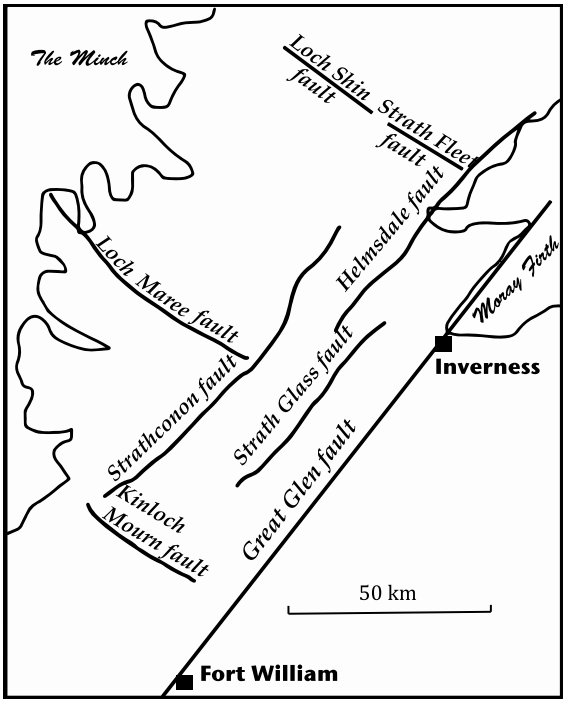

Fig. 7. Map of the crustal scale strike-slip faults of the Highlands of Scotland. The NE striking faults are left lateral, and the NW striking ones are right lateral. Based on a map in Johnstone and Mykura (1989).

This association of faults with ductile shear zones should apply only to crustal scale faults. Smaller scale faults that are entirely within the brittle regime should be expected, and are observed, to be oriented in the Coulomb manner with respect to the principal stresses, in accordance with Anderson's theory.

6. Conclusions

We modeled the evolution of shear zones/faults in the lithosphere by the localization of shear bands driven by strain weakening. The results show that shearing at all depths will either by dominated by the brittle regime in which conjugate shear planes form at the Coulomb angle or by the ductile regime in which they form at the von Mises angle. For the latter to occur requires the ductile strain weakening rate to be of order 0.2 GPa/strain or greater depending on the weakening rate in the brittle regime. The seemingly ubiquitous observation of orthogonality for low displacement crustal scale conjugate strike-slip faults requires this to be generally the case for the continents. The orthogonality of the Wharton Basin faults suggest that this may also be true of

the oceanic lithosphere. Our model also predicts, as observed, that there is no deflection of the orientation of shears at the brittle-ductile transition.

Our results explain why Anderson's theory of faulting breaks down for crustal scale faults. The different behavior of crustal scale faults was already evident in the observations presented in his 1951 book, but its significance was not understood at that time.

CRediT authorship contribution statement

Christopher Scholz conceptualized the problem, provided the geological examples and arguments and wrote the paper. Eunseo Choi developed the model, carried out all model analyses, wrote the modeling section and supplementary information and participated in discussions of all aspects of the paper.

Declaration of competing interest

The authors declare that they have no known competing financial interests or personal relationships that could have appeared to influence the work reported in this paper.

Acknowledgements

EC was supported by NSF grant No. 2104002. We thank Laetitia LePourheit and Richard Sibson for helpful reviews.

Appendix A. Supplementary material

Supplementary material related to this article can be found online at https://doi.org/10.1016/j.epsl.2021.117273.

References

Aharonov, E., Scholz, C.H., 2019. The brittle-ductile transition predicted by a physics-based friction law. J. Geophys. Res., Solid Earth 124 (3), 2721–2737. https://doi.org/10.1029/2018jb016878.

AIST, 2015. Active Fault database of Japan, edited by A. F. R. Center, National Institute of Advanced Industrial Science and Technology AIST, Geological Survey of Japan.

Aktar, M., Karabulut, H., Ozalaybey, S., Childs, D., 2007. A conjugate strike-slip fault system within the extensional tectonics of Western Turkey. Geophys. J. Int. 171 (3), 1363–1375. https://doi.org/10.1111/j.1365-246X.2007.03598.x.

Anderson, E.M., 1905. The dynamics of faulting. Trans. Edinb. Geol. Soc. 8, 387–402.

Anderson, E.M., 1951. The Dynamics of Faulting, 2nd ed. Oliver and Boyd, Edinburgh. 206 pp.

Anderson, J.L., Tolan, T.L., Wells, R.E., 2013. Strike-slip faults in the western Columbia River flood basalt province, Oregon and Washington. In: Reidel, S.P., Camp, V.E., Ross, M.E., Wolff, J.A., Martin, B.S., Tolan, T.L., Wells, R.E. (Eds.), Columbia River Flood Basalt Province, pp. 325–347.

Bonnin, M., Barruol, G., Bokelmann, G.H.R., 2010. Upper mantle deformation beneath the North American-Pacific plate boundary in California from SKS splitting. J. Geophys. Res., Solid Earth 115. https://doi.org/10.1029/2009jb006438.

Brandmayr, M., Dallmeyer, R.D., Handler, R., Wallbrecher, E., 1995. Conjugate shear zones in the Southern Bohemian Massif (Austria) - implications for Variscan and Alpine tectonothermal activity. Tectonophysics 248 (1–2), 97–116. https://doi.org/10.1016/0040-1951(95)00003-6.

Brewer, J.A., Matthews, D.H., Warner, M.R., Hall, J., Smythe, D.K., Whittington, R.J., 1983. Birps deep seismic-reflection studies of the British-Caledonides. Nature 305 (5931), 206–210. https://doi.org/10.1038/305206a0.

Byerlee, J.D., 1978. Friction of rocks. Pure Appl. Geophys. 116, 615–626.

Choi, E., Tan, E., Lavier, L.L., Calo, V.M., 2013. DynEarthSol2D: an efficient unstructured finite element method to study long-term tectonic deformation. J. Geophys. Res., Solid Earth 118 (5), 2429–2444. https://doi.org/10.1002/jgrb.50148.

Collettini, C., Tesei, T., Scuderi, M.M., Carpenter, B.M., Viti, C., 2019. Beyond Byerlee friction, weak faults and implications for slip behavior. Earth Planet. Sci. Lett. 519, 245–263. https://doi.org/10.1016/j.epsl.2019.05.011.

Di Toro, G., Han, R., Hirose, T., De Paola, N., Nielsen, S., Mizoguchi, K., Ferri, F., Cocco, M., Shimamoto, T., 2011. Fault lubrication during earthquakes. Nature 471, 494–498. https://doi.org/10.1038/nature09838.

Freund, R., 1974. Kinematics of transform and transcurrent faults. Tectonophysics 21 (1–2), 93–134.

Gueydan, F., Precigout, J., Montesi, L.G.J., 2014. Strain weakening enables continental plate tectonics. Tectonophysics 631, 189–196. https://doi.org/10.1016/j.tecto.2014.02.005.

Hatem, A.E., Dolan, J.F., 2018. A model for the initiation, evolution, and controls on seismic behavior of the Garlock Fault, California. Geochem. Geophys. Geosyst. 19 (7), 2166–2178. https://doi.org/10.1029/2017gc007349.

Hill, E.M., et al., 2015. The 2012 M(w)8.6 Wharton Basin sequence: a cascade of great earthquakes generated by near-orthogonal, young, oceanic mantle faults. J. Geophys. Res., Solid Earth 120 (5), 3723–3747. https://doi.org/10.1002/2014jb011703.

Holdsworth, R.E., et al., 2015. Silurian–Devonian magmatism, mineralization, regional exhumation and brittle strike-slip deformation along the Loch Shin Line, NW Scotland. J. Geol. Soc. (Lond.) 172, 2015–2058. https://doi.org/10.1144/jgs2015-058.

Holyoke, C.W., Tullis, J., 2006. Mechanisms of weak phase interconnection and the effects of phase strength contrast on fabric development. J. Struct. Geol. 28, 621–640. https://doi.org/10.1016/j.jsg.2006.01.008.

Hudnut, K., Seeber, L., Rockwell, T., Goodmacher, J., Klinger, R., Lindvall, S., McElwain, R., 1989. Surface ruptures on cross-faults in the 24 November 1987 Superstition Hills, California, earthquake sequence. Bull. Seismol. Soc. Am. 79 (2), 282–296.

Johnstone, J.S., Mykura, W., 1989. The Northern Highlands of Scotland. British Geological Survey, London. 219 pp.

Kelly, P.G., Sanderson, D.J., Peacock, D.C.P., 1998. Linkage and evolution of conjugate strike-slip fault zones in limestones of Somerset and Northumbria. J. Struct. Geol. 20 (11), 1477–1493. https://doi.org/10.1016/s0191-8141(98)00048-0.

Kranz, R.L., Scholz, C.H., 1977. Critical dilatant volume of rocks at the onset of tertiary creep. J. Geophys. Res. 82, 4893–4898.

Kronenberg, A.K., Kirby, S.H., Pinkston, J., 1990. Basal slip and mechanical anisotropy of biotite. J. Geophys. Res. 95, 19257–19278. https://doi.org/10.1029/JB095iB12p19257.

LeLoup, P.H., Lacassin, R., Tapponnier, P., et al., 1995. The Ailao Shan - Red River shear zone (Yunnan, China), Tertiary transform boundary of Indochina. Tectonophysics 252, 3–84. https://doi.org/10.1016/0040-1951(95)00070-4.

Liang, C., Ampuero, J.P., Pino Muñoz, D., 2021. Deep ductile shear zone facilitates near-orthogonal strike-slip faulting in a thin brittle lithosphere. Geophys. Res. Lett. 48 (2). https://doi.org/10.1029/2020GL090744.

Lockner, D.A., Byerlee, J.D., Kuksenko, V., Ponomarev, A., Sidorin, A., 1992. Quasistatic fault growth from acoustic emissions. In: Evans, B., Wong, T.-F. (Eds.), Fault Mechanics and Transport Properties of Rock. Academic Press, pp. 3–32.

Martel, S.J., 1999. Mechanical controls on fault geometry. J. Struct. Geol. 21 (6), 585–596.

Matsu'ura, M., 1977. Inversion of geodetic data. Part II. Optimal model of conjugate fault system for the 1927 Tango earthquake. J. Phys. Earth 25 (3), 233–255.

Moore, J.D.P., Parsons, B., 2015. Scaling of viscous shear zones with depth-dependent viscosity and power-law stress-strain-rate dependence. Geophys. J. Int. 202, 242–260. https://doi.org/10.1093/gji/ggv143.

Nakamura, K., 1969. Arrangement of parasitic cones as a possible key to a regional stress field. Bull. Volcanol. Soc. Jpn. 14, 8–20.

Nicholson, C., Seeber, L., Williams, P., Sykes, L.R., 1986. Seismic evidence for conjugate slip and block rotation within the San-Andreas fault system, Southern-California. Tectonics 5 (4), 629–648. https://doi.org/10.1029/TC005i004p00629.

Nixon, C.W., Sanderson, D.J., Bull, J.M., 2011. Deformation within a strike-slip fault network at Westward Ho! Devon UK: domino vs conjugate faulting. J. Struct. Geol. 33 (5), 833–843. https://doi.org/10.1016/j.jsg.2011.03.009.

Norris, R.J., Toy, V.G., 2014. Continental transforms: a view from the Alpine fault. J. Struct. Geol. 64, 3–31. https://doi.org/10.1016/j.jsg.2014.03.003.

Parsons, T., 1998. Seismic-reflection evidence that the Hayward fault extends into the lower crust of the San Francisco Bay Area, California. Bull. Seismol. Soc. Am. 88, 1212–1223.

Peacock, D.C.P., Sanderson, D.J., 1995. Strike-slip relay ramps. J. Struct. Geol. 17 (10), 1351–1360. https://doi.org/10.1016/0191-8141(95)97303-w.

Regenauer-Lieb, K., Yuen, D., 2004. Positive feedback of interacting ductile faults from coupling of equation of state, rheology and thermal-mechanics. Phys. Earth Planet. Inter. 142 (1–2), 113–135. https://doi.org/10.1016/j.pepi.2004.01.003.

Robinson, D.P., Henry, C., Das, S., Woodhouse, J.H., 2001. Simultaneous rupture along two conjugate planes of the Wharton basin earthquake. Science 292 (5519), 1145–1148. https://doi.org/10.1126/science.1059395.

Ross, Z.E., Hauksson, E., Ben-Zion, Y., 2017. Abundant off-fault seismicity and orthogonal structures in the San Jacinto fault zone. Sci. Adv. 3 (3). https://doi.org/10.1126/sciadv.1601946.

Ross, Z.E., et al., 2019. Hierarchical interlocked orthogonal faulting in the 2019 Ridgecrest earthquake sequence. Science 366 (6463), 346–351. https://doi.org/10.1126/science.aaz0109.

Rutter, E.H., 1999. On the relationship between the formation of shear zones and the form of the flow law for rocks undergoing dynamic recrystallization. Tectonophysics 303 (1–4), 147–158. https://doi.org/10.1016/s0040-1951(98)00261-3.

Rybacki, E., Dresen, G., 2000. Dislocation and diffusion creep of synthetic anorthite aggregates. J. Geophys. Res. 105, 26017–26036. https://doi.org/10.1029/2000JB900223.

Scholz, C.H., 2019. The Mechanics of Earthquakes and Faulting, 3rd ed. Cambridge Univ. Press, Cambridge. 493 pp.

Sibson, R.H., 1983. Continental fault structure and the shallow earthquake source. J. Geol. Soc. 140, 741–767. https://doi.org/10.1144/gsjgs.140.5.0741.

Simao, N.M., Nalbant, S.S., Sunbul, F., Mutlu, A.K., 2016. Central and eastern Anatolian crustal deformation rate and velocity fields derived from GPS and earthquake data. Earth Planet. Sci. Lett. 433, 89–98. https://doi.org/10.1016/j.epsl.2015.10.041.

Tan, E., Choi, E., Lavier, L., Calo, V., 2013. DynEarthSol3D: an efficient and flexible unstructured finite element method to study long-term tectonic deformation. Abstract DI31A-2197 presented at: 2013 Fall Meeting, AGU, San Francisco, Calif., 9-13 Dec.

Thatcher, W., Hill, D.P., 1991. Fault orientations in extensional and conjugate strike-slip environments and their implications. Geology 19 (11), 1116–1120. https://doi.org/10.1130/0091-7613(1991)019<1116:foieac>2.3.co;2.

Townend, J., 2006. What do faults feel? Observational constraints on the stresses acting on seismogenic faults. In: Abercrombie, A.M.R., Di Toro, G., Kanamori, H. (Eds.), Earthquakes: Radiated Energy and the Physics of Faulting. In: Geophys. Monographs, vol. 170. Amer. Geophys. Union, Washington, D.C., pp. 313–327.

Traore, N., LePourheit, L., Frela, J., Rolandone, F., Meyer, B., 2014. Does interseismic strain localization near strike-slip faults result from boundary conditions or rheological structure? Geophys. J. Int. 197 (1), 50–62. https://doi.org/10.1093/gji/ggu011.

Tsuboi, C., 1933. Investigation of deformation of the crust found by precise geodetic means. Jpn. J. Astron. Geophys. 10, 93–248.

Vauchez, A., Tommasi, A., Mainprice, D., 2012. Faults (shear zones) in the Earth's mantle. Tectonophysics 558, 1–27. https://doi.org/10.1016/j.tecto.2012.06.006.

Watson, J.V., 1984. The Ending of the Caledonian Orogeny in Scotland: President's Anniversary Address 1983. J. Geol. Soc. (Lond.) 141, 193–214.

Yamasaki, T., Wright, T.J., Houseman, G.A., 2014. Weak ductile shear zone beneath a major strike-slip fault: inferences from earthquake cycle model constrained by geodetic observations of the western North Anatolian fault zone. J. Geophys. Res., Solid Earth 119 (4), 3678–3699. https://doi.org/10.1002/2013jb010347.

Yue, H., Lay, T., Koper, K.D., 2012. En echelon and orthogonal fault ruptures of the 11 April 2012 great intraplate earthquakes. Nature 490 (7419), 245–249. https://doi.org/10.1038/nature11492.